End-To-End Trajectory Design for a Solar-Sail-Only Pole-Sitter at Venus, Earth, and Mars

Jeannette Heiligers[a,1], *Merel Vergaaij*[b], *Matteo Ceriotti*[b]

[a]*Faculty of Aerospace Engineering, Delft University of Technology, 2652 HS Delft, The Netherlands*

[b]*James Watt School of Engineering, University of Glasgow, Glasgow G12 8QQ, United Kingdom*

Abstract

The concept of a pole-sitter has been under investigation for many years, showing the capability of a low-thrust propulsion system to maintain a spacecraft at a static position along a planet's polar axis. From such a position, the spacecraft has a view of the planet's polar regions equivalent to that of the low- and mid-latitudes from geostationary orbit. Previous work has hinted at the existence of pole-sitters that would only require a solar sail to provide the necessary propulsive thrust if a slight deviation from a position exactly along the polar axis is allowed, without compromising on the continuous view of the planet's polar region (a so-called quasi-pole-sitter). This paper conducts a further in-depth analysis of these high-potential solar-sail-only quasi-pole-sitters and presents a full end-to-end trajectory design: from launch and transfer to orbit design and orbit control. The results are the next steppingstone towards strengthening the feasibility and utility of these orbits for continuous planetary polar observation.

Keywords: Solar sailing, Pole-sitter, Orbit design, Trajectory optimisation, Orbit control

1. Introduction

The concept of a pole-sitter comprises a single spacecraft to provide continuous coverage of the northern latitudes of a planet (Ceriotti, Heiligers and McInnes 2014, Walmsley, Heiligers, Ceriotti et al. 2016) or moon (Grebow, Ozimek and Howell 2008) to support planetary sciences, weather forecasting, and commercial services such as telecommunication. The idea of the pole-sitter concept originated from the existence of artificial equilibrium points in the circular restricted three-body problem (CRTBP) (Driver 1980, Golan and Breakwell 1988), which appear when the CRTBP is complemented with an acceleration produced by low-thrust propulsion. Then, the five Lagrange points of the classical (i.e. no-propulsion) CRTBP extend into an infinite set of artificial equilibrium points, including equilibria above and below the orbital plane of the two primaries (McInnes 1999).

[1] Corresponding author, m.j.heiligers@tudelft.nl

However, from these equilibrium points, continuous, year-long coverage of the polar regions of a planet cannot be guaranteed due to the body's obliquity, i.e. the angle between its orbital and equatorial planes.

To ensure the desired continuous observation, research in recent years has shifted from aiming to maintain a spacecraft around an equilibrium point to maintaining a spacecraft along the planet's polar axis. For this, the spacecraft needs to be equipped with a low-thrust propulsion system to counteract the gravitational attraction of the planet as well as that of other significant celestial bodies. For example, for a pole-sitter at Earth, the Sun exerts a non-negligible gravitational acceleration on the spacecraft. Both solar-electric propulsion (SEP) and a hybrid propulsion system consisting of SEP and solar sailing have been proposed as suitable propulsion methods (Ceriotti, Heiligers and McInnes 2014, Heiligers, van den Oever, Ceriotti et al. 2017). As part of the hybrid option, the solar sail is used as a means to limit the propellant consumption by the SEP thruster and thus to extend the mission lifetime and/or increase the payload capability, while the SEP thruster can provide (part of) the necessary acceleration when the solar sail is unable to do so. Such hybrid-propulsion pole-sitters at Earth have been investigated extensively, from the orbit design (Ceriotti and McInnes 2011, Ceriotti, Heiligers and McInnes 2014, Heiligers, Ceriotti, McInnes et al. 2014), to transfers from Earth to reach the pole-sitter orbit (Heiligers, Ceriotti, McInnes et al. 2012), to orbit control (Ceriotti and McInnes 2010), and payload design (Ceriotti, Heiligers and McInnes 2014), as well as transfers between pole-sitters above the North and South Pole (Heiligers, Ceriotti, McInnes et al. 2012). The pole-sitter concept has also been extended to other planets, including Venus and Mars, indicating that Mars is a very suitable planet for a pole-sitter mission due to its low mass and relatively far distance from the Sun (Walmsley, Heiligers, Ceriotti et al. 2016).

In an attempt to further reduce the propellant consumption by the SEP thruster, a recent study has investigated the possibility to loosen the requirement that the spacecraft needs to be maintained *exactly* along the polar axis at all times. Indeed, by redefining the constraint such that the spacecraft always needs to be in view of the entire polar region (i.e. it needs to achieve a certain elevation angle for all locations above a predefined latitude), further gains in propellant consumption can be achieved (Heiligers, van den Oever, Ceriotti et al. 2017). In fact, initial results in (Heiligers, van den Oever, Ceriotti et al. 2017) showed that for elevation angles up to approximately 30 deg, the propellant consumption may even be reduced to zero, indicating the fact that these so-called quasi-pole-sitter orbits could be maintained using solar-sail propulsion *only*. Note that from here on, for brevity, the prefix "quasi-" in the term "quasi-pole-sitters" will be omitted.

This paper builds on these initial results and conducts the first-ever thorough investigation into solar-sail-only pole-sitters at Venus, Earth, and Mars. In particular, instead of finding these orbits through a hybrid-propulsion approach to find zero-propellant solutions, this paper adopts a solar-sail-only approach. The adopted approach starts from solar-sail periodic orbits around out-of-plane equilibria. Though these orbits do not satisfy the viewing requirements of the pole-sitter, they can be

used as seed in an optimisation algorithm to impose those viewing requirements. In addition, transfer trajectories from an Earth geostationary transfer orbit (GTO) to the found pole-sitter orbits are investigated as well as an analysis to control the transfer trajectories and pole-sitter orbits under unaccounted dynamical perturbations and guidance errors. As such, this paper presents an end-to-end trajectory design for solar-sail-only pole-sitters at Venus, Earth, and Mars.

After this introduction, the paper continues with an overview of the dynamics and constraints involved in the design of the pole-sitter concept. Subsequently, Section 3 presents a detailed analysis of the orbit design of the solar-sail-only pole-sitters and draws conclusions on the solar-sail technology required to achieve a certain minimum elevation angle at any location inside a planet's Artic circle. Here, a "minimum" elevation angle indicates that an observer at any location inside a planet's Arctic circle has a continuous line of sight with the spacecraft, where the spacecraft is at an elevation angle equal to or larger than the minimum elevation angle. Subsequently, for a subset of orbits, the solar-sail trajectory from GTO to the pole-sitter orbits is designed and optimised for minimum time of flight, see Section 4. Finally, in Section 5, a study into the orbit control of both the transfer trajectory and pole-sitter orbit is presented, showing a statistical analysis on the size of injection errors from which the spacecraft can still recover. The paper ends with the conclusions in Section 6.

2. Dynamics

This section will start with a definition of the dynamical framework in which the pole-sitter orbits, the transfer trajectories towards the orbits as well as the trajectory and orbit control are designed, see Section 2.1. Section 2.2 will subsequently describe the two different solar-sail reflectance models applied in this paper. Finally, in Section 2.3, the pole-sitter constraint that ensures the viewing requirements (as defined in the introduction) will be derived.

2.1. Solar-sail augmented circular restricted three-body problem

The dynamical framework adopted in this paper is that of the circular restricted three-body problem (CRTBP), augmented with the acceleration induced by a solar sail. As a result, the motion of the spacecraft is assumed to be affected only by the gravitational attraction of two large celestial bodies (in this paper the Sun and planet under consideration) and the solar radiation pressure acceleration. The spacecraft itself exerts no gravitational acceleration on the large celestial bodies, which are assumed to move in circular orbits around their barycentre. Note that the small eccentricities of the orbits of the planets under investigation in this paper, see Table 1, justify the latter assumption. Furthermore, canonical units are used, where the Sun-planet distance is taken as the unit of distance, λ , the Sun-planet system mass is taken as the unit of mass, and the unit of time is chosen such that the orbital period of the system is 2π. Values for these units can be found in

Table 1, where the unit of mass is expressed through the mass ratio, $\mu = m_P / (m_S + m_P)$, with m_P and m_S the masses of the planet and Sun, respectively.

Table 1 Orbital characteristics of Venus, Earth, and Mars and fundamental CRTBP parameters for each Sun-planet system.

	Venus	Earth	Mars
Orbit eccentricity	0.007	0.0167	0.0934
Unit of distance, λ [km]	1.0821×10^8	1.4960×10^8	2.2794×10^8
Mass ratio, μ	2.4476×10^{-6}	3.0404×10^{-6}	3.2268×10^{-7}
Unit of time [s]	3.0897×10^6	5.0224×10^6	9.4461×10^6
Planet radius, $R_{P,\mathrm{dim}}$ [km]	6051.8	6378.2	6378.2
Obliquity, δ_{eq} [deg]	177.36	23.5	25.19

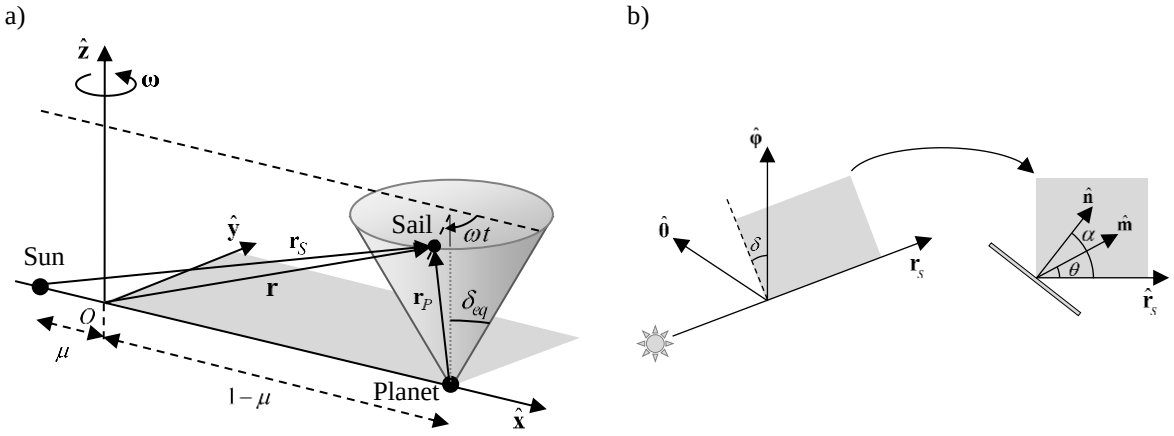

Figure 1 a) Definition of synodic reference frame *A* and polar axis conical motion, b) definition of reference frame *B* and solar-sail control angles, adapted from (Ceriotti and McInnes 2011).

To describe the spacecraft dynamics, a Sun-planet synodic reference frame, $A(\hat{\mathbf{x}}, \hat{\mathbf{y}}, \hat{\mathbf{z}})$, centred at the system's barycentre is adopted, where the basis vector $\hat{\mathbf{x}}$ points along the Sun-planet line towards the planet, the $\hat{\mathbf{z}}$-vector points along the planet's orbital angular momentum vector, and the $\hat{\mathbf{y}}$-vector completes the right-handed reference frame, see Figure 1a. In this reference frame, the spacecraft equations of motion are defined as (McInnes 1999):

$$\ddot{\mathbf{r}} + 2\boldsymbol{\omega} \times \dot{\mathbf{r}} = \mathbf{a}_s - \nabla U \tag{1}$$

with $\mathbf{r} = \begin{bmatrix} x & y & z \end{bmatrix}^T$ the spacecraft's dimensionless position vector, $\boldsymbol{\omega} = \omega \hat{\mathbf{z}} = \begin{bmatrix} 0 & 0 & 1 \end{bmatrix}^T$ the dimensionless rotation rate of the reference frame, $\mathbf{a}_s$ the dimensionless solar-sail induced acceleration vector (which will be defined in Section 2.2), and U the so-called effective potential. The effective potential combines the gravitational and centrifugal potentials as

$U = -\frac{1}{2}\left(x^2 + y^2\right) - \left(\left[1-\mu\right]/r_S + \mu/r_P\right)$ where r_S and r_P are the dimensionless Sun-sail and planet-sail distances, see Figure 1a. These distances are defined as $r_S = \|\mathbf{r}_S\| = \left\|\begin{bmatrix} x+\mu & y & z \end{bmatrix}^T\right\|$ and $r_P = \|\mathbf{r}_P\| = \left\|\begin{bmatrix} x-(1-\mu) & y & z \end{bmatrix}^T\right\|$, respectively.

2.2. Solar-sail induced acceleration

To model the solar-sail induced acceleration (from here on, in short referred to as the sail acceleration), this paper considers two sail reflectance models: 1) a low-fidelity ideal reflectance model, where all photons are assumed to be specularly reflected by the sail, and 2) a higher-fidelity non-ideal reflectance model that also accounts for diffuse reflection, absorption, and thermal emission. Both models can be captured in the following definition of the sail acceleration (Ceriotti and McInnes 2011):

$$\mathbf{a}_s = \frac{\beta}{2}\frac{1-\mu}{r_P^2}\sqrt{\left[\frac{f_N}{PA}\right]^2 + \left[\frac{f_T}{PA}\right]^2}\,\hat{\mathbf{m}} \tag{2}$$

In Eq. (2), $\hat{\mathbf{m}}$ is the direction of the sail acceleration and β is the solar-sail lightness number, which is defined as the ratio of the solar radiation pressure acceleration to the solar gravitational acceleration. With previous and planned solar-sail missions reaching lightness numbers of up to 0.015 (e.g. IKAROS: $\beta = 0.001$ (Mori, Shirasawa, Mimasu et al. 2013), NanoSail-D2: $\beta = 0.003$ (Johnson, Whorton, Heaton et al. 2011), LightSail-1: $\beta = 0.011$ (Biddy and Svitek 2012), and NEA Scout: $\beta = 0.010$ (Heaton, Ahmad and Miller 2017)) and estimates for near-term solar-sail technology reaching $\beta = 0.04$ (Heiligers, Fernandez, Stohlman et al. 2019), this paper will consider a lightness number range of up to $\beta = 0.1$ to also reflect solar-sail technology expected in the far-term (Dachwald 2005). Returning to Eq. (2), P is the solar radiation pressure, A the sail area, and f_N and f_T the magnitudes of the solar radiation pressure forces acting normal and tangential to the sail, respectively. The latter are defined as:

$$f_N = PA\left[\left(1+\tilde{r}s\right)\cos^2\alpha + B_f\left(1-s\right)\tilde{r}\cos\alpha + \left(1-\tilde{r}\right)\frac{\varepsilon_f B_f - \varepsilon_b B_b}{\varepsilon_f + \varepsilon_b}\cos\alpha\right] \tag{3}$$

$$f_T = PA\left(1-r\tilde{s}\right)\cos\alpha\sin\alpha \tag{4}$$

In Eqs. (3) and (4), $\tilde{r}$, s, B, and ε are the reflectance properties of the front (subscript 'f') and back (subscript 'b') of the solar sail: the total reflectivity constant, the specular reflectivity fraction coefficient, the non-Lambertian coefficient, and the emissivity coefficient, respectively. Values for these properties for both an ideal and a non-ideal sail reflectance model can be found in Table 2.

Finally, α is the cone angle of the sail, which is defined as the angle between the sail normal vector, $\hat{\mathbf{n}}$, and the direction of sunlight, $\hat{\mathbf{r}}_S$, see Figure 1b.

Table 2 Solar-sail reflectance coefficients (Heaton, Ahmad and Miller 2017).

Model	$\tilde{r}$	s	B_f	B_b	ε_f	ε_b
Ideal	1	1	n/a	n/a	n/a	n/a
Non-ideal	0.91	0.94	0.79	0.67	0.025	0.27

In order to uniquely define $\hat{\mathbf{n}}$, a sail-centred reference frame $B\left(\hat{\mathbf{r}}_S, \hat{\boldsymbol{\theta}}, \hat{\boldsymbol{\varphi}}\right)$ is employed where $\hat{\boldsymbol{\theta}} = \left(\hat{\mathbf{z}} \times \hat{\mathbf{r}}_S\right) / \left\|\hat{\mathbf{z}} \times \hat{\mathbf{r}}_S\right\|$ and $\hat{\boldsymbol{\varphi}} = \hat{\mathbf{r}}_S \times \hat{\boldsymbol{\theta}}$, see Figure 1b. Within frame B and using the cone and clock angles, α and δ (see again Figure 1b), the normal vector can be defined as:

$$\hat{\mathbf{n}}^{(B)} = \begin{bmatrix} \cos\alpha & \sin\alpha\sin\delta & \sin\alpha\cos\delta \end{bmatrix}^T \tag{5}$$

where the superscript (B) indicates that $\hat{\mathbf{n}}$ is defined in frame B. Note that the clock angle is defined as the angle between the projection of $\hat{\mathbf{n}}^{(B)}$ onto the $\left(\hat{\boldsymbol{\theta}}, \hat{\boldsymbol{\varphi}}\right)$-plane and the basis vector $\hat{\boldsymbol{\varphi}}$.

For an ideal sail reflectance model, it follows from Eqs. (3) and (4) and the coefficients in the first row of Table 1 that $f_N = 2PA\cos^2\alpha$ and $f_T = 0$. The latter thus implies that, for the case of an ideal reflectance model, the sail acceleration acts along the sail normal vector, i.e. $\hat{\mathbf{m}} = \hat{\mathbf{n}}$, and Eq. (2) reduces to:

$$\mathbf{a}_s = \beta \frac{1-\mu}{r_P^2} \cos^2\alpha \hat{\mathbf{n}} \tag{6}$$

Instead, for a non-ideal sail reflectance model, $f_T \neq 0$, which implies that $\hat{\mathbf{m}} \neq \hat{\mathbf{n}}$ and the equivalent of the cone angle for vector $\hat{\mathbf{m}}$ becomes:

$$\theta = \alpha - \xi = \alpha - \tan^{-1}\left(f_T / f_N\right) \tag{7}$$

The sail acceleration direction, $\hat{\mathbf{m}}$, in frame B can then be expressed as:

$$\hat{\mathbf{m}}^{(B)} = \begin{bmatrix} \cos\theta & \sin\theta\sin\delta & \sin\theta\cos\delta \end{bmatrix}^T \tag{8}$$

A transformation in the form of

$$\hat{\mathbf{m}}^{(A)} = \begin{bmatrix} \hat{\mathbf{r}}_S^{(A)} & \hat{\boldsymbol{\theta}}^{(A)} & \hat{\boldsymbol{\varphi}}^{(A)} \end{bmatrix} \hat{\mathbf{m}}^{(B)} \tag{9}$$

finally provides the sail acceleration direction in the correct reference frame for use in Eqs. (1) and (2).

2.3. Pole-sitter constraint

Due to the planet's obliquity, i.e. the angle between the planet's orbital plane and its equatorial plane, the polar axis of the planet describes a clockwise conical motion in frame A, see Figure 1a. From a planet-centred perspective, i.e. translating the origin of frame A from the barycentre to the planet's centre of mass, the direction of this polar axis, $\hat{\mathbf{p}}$, varies over time according to:

$$\hat{\mathbf{p}}(t) = \begin{bmatrix} \sin\delta_{eq}\cos\omega t \\ -\sin\delta_{eq}\sin\omega t \\ \cos\delta_{eq} \end{bmatrix} \tag{10}$$

such that $t = 0$ corresponds to the winter solstice, see also Figure 1a. In this paper, the spacecraft is required to track the motion of this polar axis, but is at the same time allowed to move around the polar axis as long as it can observe any location on the planet above a minimum latitude, $\delta_{\min}$, at a minimum elevation angle, $\gamma_{\min}$. Note that, the larger this minimum elevation angle, the better the quality of the observations. This constraint is visualised in Figure 2a and can be expressed through an observation angle, ϕ, as:

$$\phi = \cos^{-1}\left(\hat{\mathbf{p}}\cdot\hat{\mathbf{r}}_A\right) \le \phi_{\max} = \delta_{\min} - \gamma_{\min} \tag{11}$$

where $\hat{\mathbf{r}}_A$ is the unit vector pointing from the apex of the cone in Figure 2a to the spacecraft. Again, from a planet-centred perspective, this unit vector can be expressed as (Heiligers, van den Oever, Ceriotti et al. 2017):

$$\hat{\mathbf{r}}_A = \frac{\mathbf{r}_P - h_P\hat{\mathbf{p}}}{\left\|\mathbf{r}_P - h_P\hat{\mathbf{p}}\right\|},\ h_p = \frac{\sin\left(90^o + \gamma_{\min}\right)}{\sin\left(\delta_{\min} - \gamma_{\min}\right)}R_P \tag{12}$$

with $R_P = R_{P,\dim}/\lambda$ the planet's dimensionless radius. Values for both $R_{P,\dim}$ and λ can be found in Table 1. As an example, the blue cones in Figure 2b (superimposed on the polar axis cone) show the allowable motion around the Earth's polar axis at four epochs during the year (at winter, spring, summer and autumn) and for $\delta_{\min} = 65.8$ deg and a minimum elevation angle of $\gamma_{\min} = 60$ deg. These values represent the condition that any location within the Arctic region (starting at $\delta_{\min} = 65.8$ deg) should be visible at a minimum elevation angle of 60 deg. Note that, for comparison purposes in this paper, the same minimum latitude of $\delta_{\min} = 65.8$ deg is adopted for all planets.

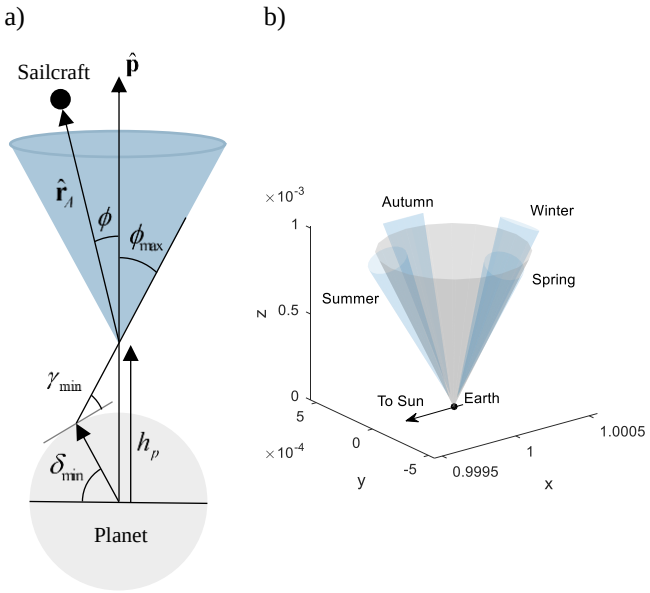

Figure 2 a) Schematic of the pole-sitter constraint, b) allowable deviation from Earth's polar axis during winter, spring, summer and autumn for $\delta_{\min} = 65.8$ deg and $\gamma_{\min} = 60$ deg (Heiligers, van den Oever, Ceriotti et al. 2017).

3. Orbit design

The goal of this paper is to find orbits that: 1) satisfy the pole-sitter constraint in Eq. (11), 2) have a period of one planetary year such that they can be repeated over time, and 3) remain as close as possible to the planet to maximise the spatial resolution of the observations or minimise the path loss for telecommunications. In order to find such orbits, the problem is formulated as an optimal control problem, which is defined in Section 3.1 and solved using a direct pseudo-spectral method, which is discussed in Section 3.2. An initial guess to initialise the optimisation is discussed in Section 3.3 and the results are presented in Section 3.4.

3.1. *Optimal control problem*

The objective of the optimal control problem is to find the states $\mathbf{x}(t) = \begin{bmatrix} x & y & z & v_x & v_y & v_z \end{bmatrix}^T$ and controls $\mathbf{u}(t) = \begin{bmatrix} \alpha & \delta \end{bmatrix}^T$ over time that abide by the dynamics in Eq. (1) and minimise the distance to the planet along the pole-sitter orbit:

$$J_1 = \int_{t_0=0}^{t_f=2\pi} \left\| \mathbf{r}_P(t) \right\| dt \tag{13}$$

In addition, for the orbits to be one-planetary year periodic, the initial and final (dimensionless) times are constrained as $t_0 = 0$, $t_f = 2\pi$ and the initial and final state vectors are forced to coincide,

i.e. $\mathbf{x}(t_0) = \mathbf{x}(t_f)$. Note that, to aid convergence, $y(t_0) = 0$ is defined such that, at winter solstice, the spacecraft is located along the $\hat{\mathbf{x}}$-axis. Finally, the pole-sitter constraint of Eq. (11) is imposed on the orbit.

Suitable bounds are imposed on the state and control variables, where the latter are defined as:

$$\begin{aligned} \begin{bmatrix} 0^o \\ 0^o \end{bmatrix} \le \mathbf{u}(t) \le \begin{bmatrix} 70^o \\ 360^o \end{bmatrix} \quad &\text{Venus} \\ \begin{bmatrix} 0^o \\ -180^o \end{bmatrix} \le \mathbf{u}(t) \le \begin{bmatrix} 70^o \\ 180^o \end{bmatrix} \quad &\text{Earth/Mars} \end{aligned} \tag{14}$$

Because a solar sail cannot generate an acceleration with a component in the direction of the Sun, the cone angle is usually defined in the range $\alpha \le 90$ deg. However, it is known that control of the sail attitude is not guaranteed for very large cone angles ($\alpha > 70$ deg (Heaton, Ahmad and Miller 2017)). Therefore, in this work, a maximum cone angle of 70 deg is adopted. Regarding the bounds on the clock angle in Eq. (14), initial results showed that different bounds for the three different planet cases appeared beneficial to avoid sudden changes in the control history which could hinder the convergence of the algorithm: while the clock angle for the Venus case oscillates around a value of 180 deg, the clock angle oscillates around a value of 0 deg for the Earth and Mars cases, see also Section 3.4.2.

3.2. Optimal control solver

The optimal control problem defined in Section 3.1 is solved numerically using a direct method based on pseudospectral transcription, implemented in the software tool PSOPT (Becerra 2010). The resulting non-linear programming (NLP) problem is solved through IPOPT (Wächter and Biegler 2006), an open source C++ implementation of an interior point method for large-scale problems. PSOPT is written in C++ by V.M. Becerra and is free and open source. PSOPT can deal with all constraints defined in Section 3.1, i.e. endpoint constraints, path constraints, bounds on the states and controls and can optimise both Mayer- and Lagrange-type objective functions. The user can define the number of collocation points and indicate whether or not a mesh refinement needs to be executed. For the orbit design, a mesh refinement of [75, 100] nodes is adopted, with a maximum number of iterations per mesh refinement of 1000 and an NLP tolerance of 10^{-6}.

3.3. Initial guess

To initialise the optimisation, PSOPT needs an initial guess of the solution. In this paper, that initial guess is provided in the form of periodic orbits around solar-sail artificial equilibria.

3.3.1. Solar-sail artificial equilibria

From the literature it is well-known that the addition of a sail acceleration to the CRTBP dynamics transforms the five distinct Lagrange points of the classical (i.e. no-propulsion) CRTBP into three-dimensional surfaces of infinite artificial equilibria. Each equilibrium surface is characterised by a required solar-sail lightness number.

An (x, z)-cross-section of these surfaces for the Sun-Earth system is provided in Figure 3a, where the coloured lines indicate contours of equal lightness number. The solid black line indicates the orientation of the polar axis at summer solstice, while the dashed black lines represent the edge of the cone around the polar axis (see Figure 2) in which the spacecraft is allowed to move to ensure a minimum elevation angle of $\gamma_{\min} = 10$ deg. The lightness number required to maintain an equilibrium along the *sunward* dashed black line is provided in Figure 3b, clearly showing a minimum in the required lightness number for $z = 0.002$ at $\beta = 0.017$. Details for the actual equilibria selected in this work can be found in Table 3 for Earth as well as Venus and Mars. Note that, for these latter two cases, the same approach as described for Earth is used, only accounting for the correct obliquities of Venus and Mars as provided in Table 1.

3.3.2. Periodic orbits around solar-sail equilibria

From the literature (Baoyin and McInnes 2006, Waters and McInnes 2007, Heiligers, Diedrich, Derbes et al. 2014) it is known that periodic orbits exist around the equilibria found in Section 3.3.1. These periodic orbits can be found by fixing the attitude of the sail to the one of the equilibrium point, see the cone and clock angles in the last two columns of Table 3, and using the Lindstedt-Poincaré method to find the third-order solution to the linearised dynamical system. Details on the method can be found in (Baoyin and McInnes 2006, Waters and McInnes 2007, Heiligers, Diedrich, Derbes et al. 2014).

Due to the linearisation, the initial conditions of the orbit resulting from the Lindstedt-Poincaré method quickly diverge when they are propagated under the full non-linear dynamics of Eq. (1). A differential correction scheme, see (Howell 1983), is therefore employed to iteratively correct the initial conditions (keeping the z-amplitude fixed) such that the orbits are periodic under the dynamics of Eq. (1).

For all planets, a z-amplitude of 0.001 in dimensionless units is used. The resulting orbit around the equilibrium point for the Earth case is depicted in Figure 4a, with the time history of the observation angle, ϕ, see Eq. (11), in Figure 4b. From the latter figure it is clear that the periodic solar-sail orbit does not comply with the pole-sitter constraint in Eq. (11) nor with an orbit period of one planetary year (i.e. 2π). However, this initial guess (and similar initial guesses for the Venus and Mars cases) appeared to be of sufficient quality for the optimal control solver to converge to a solution satisfying all constraints.

a) b)

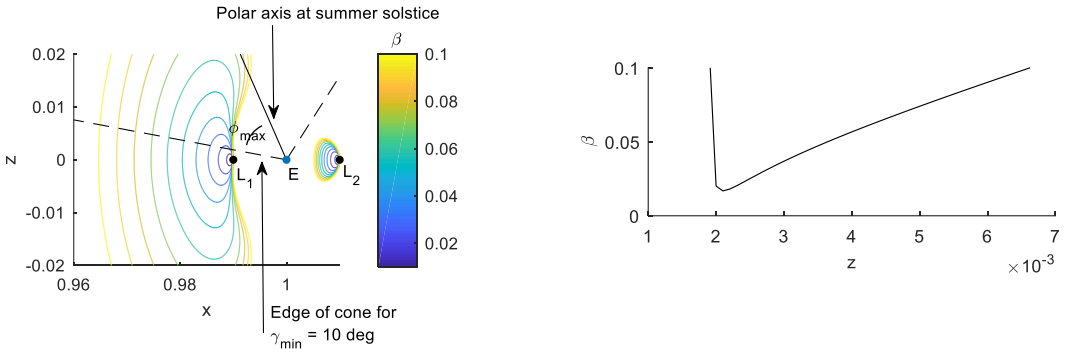

Figure 3 **Earth case**: a) contours of artificial equilibrium points for constant lightness number, β, b) lightness number as a function of z -coordinate along the sunward dashed black line in plot a).

Table 3 Details of artificial equilibria along dashed black line of Figure 3a (or equivalent for Venus and Mars) used for the generation of solar-sail periodic orbits in Section 3.3.2.

	x	z	β	α, deg	δ, deg
Venus	0.98798	-0.0090	0.041	29.8	180
Earth	0.97354	0. 0050	0.074	4.5776	0
Mars	0.98423	0.0025	0.046	3.4486	0

a) b)

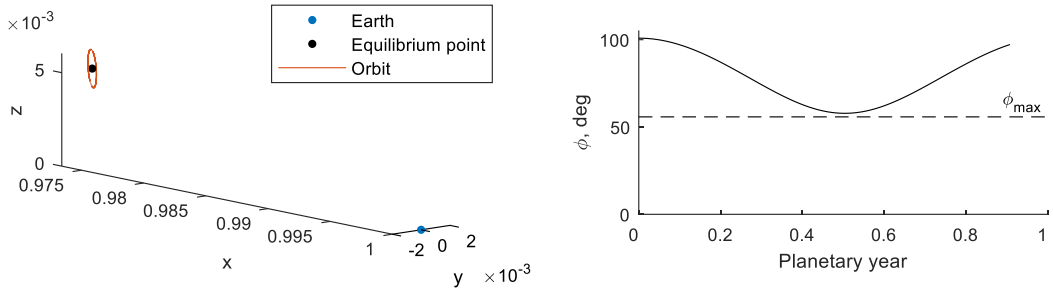

Figure 4 **Earth case**: solar-sail periodic orbit around equilibrium point of Table 3, a) orbit, b) observation angle over time.

3.4. Continuation approach

The introduction of Section 3 outlined three criteria that the pole-sitter orbits should abide by: satisfy the pole-sitter constraint in Eq. (11); be one-planetary year periodic; and remain as close as possible to the planet. This section adds a fourth criterion, namely the pole-sitter orbit should enable a minimum elevation angle, $\gamma_{\min}$, at the smallest lightness number possible, $\beta_{\min}$. To satisfy this criterion, a continuation approach is adopted. The equilibria in Table 3 (and corresponding periodic

orbits in Section 3.3.2) have been obtained for a minimum elevation angle of $\gamma_{\min} = 10$ deg. The corresponding lightness numbers are also provided in Table 3, but these are expected to be larger than what is needed for the pole-sitter orbit to achieve that minimum elevation angle. Therefore, the following stepwise continuation approach is adopted, which is schematically illustrated in Figure 5:

1) Step 1 - indicated by "start" in Figure 5

The orbits from Section 3.3.2 are taken as an initial guess for PSOPT and the optimal control problem of Section 3.1 is solved using the lightness number as indicated in Table 3, denoted as β_1, and a minimum elevation angle of $\gamma_{\min,1} = 10$ deg.

2) Step 2 - indicated by red arrow in Figure 5

The result of Step 1 is taken as an initial guess, $\gamma_{\min}$ is fixed to $\gamma_{\min,1}$ and the lightness number is reduced to $\beta_2 = \beta_1 - 0.005$. The result of this step is taken as initial guess to reduce the lightness number by another $\Delta\beta = 0.005$ and this is repeated i.e. $\beta_i = \beta_{i-1} - \Delta\beta$, until PSOPT no longer converges.

3) Step 3 – indicated by blue arrow in Figure 5

Taking the last converged solution from Step 2 as initial guess, the lightness number is now fixed to β_i and the minimum elevation angle is iteratively increased by $\Delta\gamma_{\min} = 2.5^o$, i.e. $\gamma_{\min,i} = \gamma_{\min,i-1} + \Delta\gamma_{\min}$, until PSOPT no longer converges.

4) Step 4 – indicated by green arrow in Figure 5

Taking the last converged solution from Step 3, $\gamma_{\min}$ is fixed to $\gamma_{\min,i}$ and the lightness number is iteratively increased by $\Delta\beta$, until PSOPT no longer converges.

Subsequently, Steps 3 and 4 are repeated until a maximum lightness number of $\beta = 0.1$ is reached.

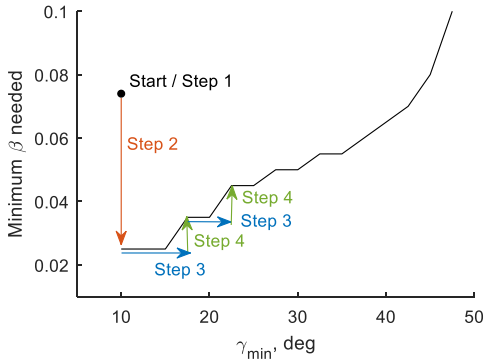

Figure 5 Schematic of the continuation approach.

3.5. Results

This section presents the pole-sitter orbits obtained through the continuation approach outlined in the previous section. Results will be presented for both the ideal and non-ideal sail reflectance models

detailed in Section 2.2. Starting with the pole-sitters for an ideal reflectance model, the overall results are shown as solid black lines in Figure 6. These solid black lines provide the smallest lightness number for which a certain minimum elevation angle can be achieved. For example, for Earth, a value for $\gamma_{\min}$ of 10 deg can be achieved for a lightness number of 0.025. This value is much smaller than the lightness number used for the initial guess of $\beta = 0.074$, see Table 3, and is the result of "Step 2" in the continuation approach of Figure 5.

By using the same scales on the horizontal and vertical axes, it is immediately clear from Figure 6 that Mars requires the smallest lightness numbers to achieve a particular $\gamma_{\min}$, followed by Earth, while Venus presents the most difficult case for the solar-sail-only pole-sitters. This conclusion is in line with preliminary results presented in (Heiligers, van den Oever, Ceriotti et al. 2017). The figure furthermore demonstrates that, for an ideal sail reflectance model, a minimum elevation angle of 47.5 deg can be achieved for Venus and Earth for $\beta \geq 0.09$, while at Mars a value of $\gamma_{\min} = 50$ deg can be achieved for $\beta \geq 0.07$. Note that, in the "true" pole-sitter scenario, where $\phi_{\max} = 0$ deg and the spacecraft is always aligned with the polar axis, the minimum elevation angle is equal to $\gamma_{\min} =$ 65.8 deg. From the results in Figure 6 it is thus clear that a solar-sail-only spacecraft cannot maintain a true pole-sitter orbit without support from an additional, propellant-consuming form of propulsion like a solar-electric propulsion thruster, which in turn will limit the mission lifetime. However, the results in Figure 6 show that, for a reduction in the minimum elevation of 15.8 – 18.3 deg, this dependency on a finite amount of onboard propellant can be entirely removed.

The orbits corresponding to the results in Figure 6 appear in Figure 7. Note that, in Figure 7, the scale on the axes is not the same for each of the three different planets. Therefore, Figure 8 is included such that the (optimised) planet-spacecraft distance can be compared among the three cases. Note that, this time, the scale on the axes *is* the same. Figure 8 clearly demonstrates that Mars is not only a favourable planet from a lightness number point of view or minimum elevation angle, but also from the point of view of the planet-spacecraft distance. Also Venus shows favourable planet-spacecraft distances (at the same order of magnitude as Mars) but with even less variation during the year which may prove even more advantageous for conducting scientific observations. Although planet-spacecraft distances are in the order of 10^6 km, an initial payload design in (Ceriotti, Heiligers and McInnes 2014) has shown that a set of instruments used on the Galileo mission and others designed for the Deep Space Climate Observatory Earth (DSCOVR)[2] mission at the Sun-Earth L_1 point enables the observation of largescale rapidly changing weather phenomena, auroras, ice-pack dynamics, and other phenomena that require only modest spatial resolution. In the same article, it was also shown that a high-gain antenna onboard an Earth pole-sitter spacecraft may be employed for a continuous data relay with scientific stations in the Antarctic and other high-latitude users.

[2] DSCOVR: Deep Space Climate Observatory https://www.nesdis.noaa.gov/content/dscovr-deep-space-climate-observatory, Accessed 22 April 2020

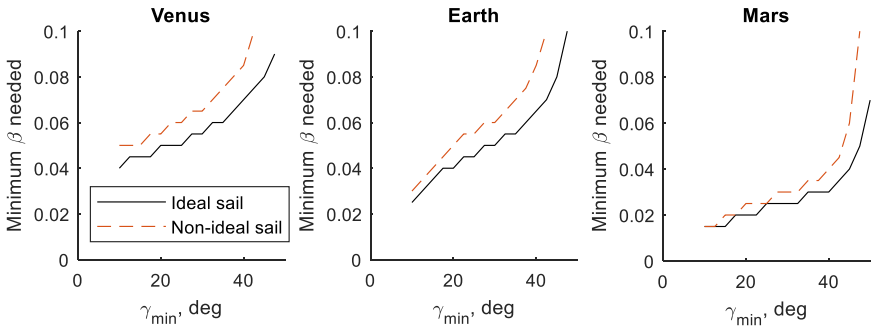

Figure 6 Minimum lightness number, β, needed to achieve a particular minimum elevation angle, $\gamma_{\min}$, at any location above a latitude of 65.8 deg for both an ideal and non-ideal sail reflectance model.

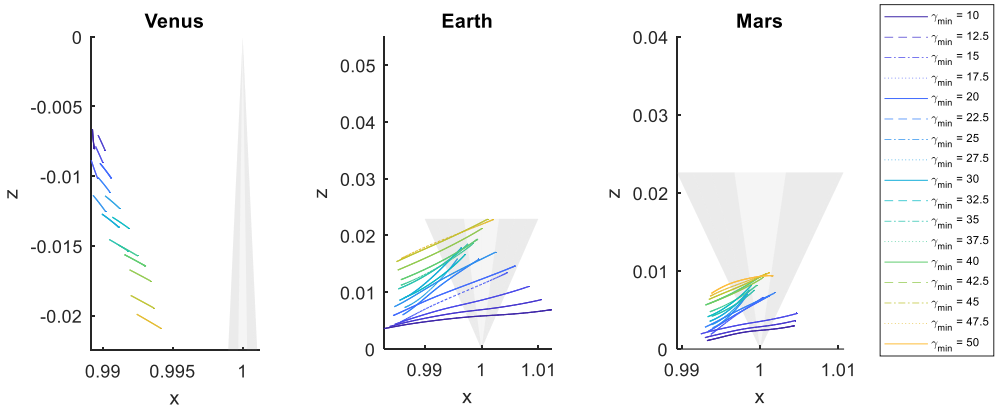

Figure 7 Pole-sitter orbits for an ideal sail reflectance model for the combinations of lightness number and minimum elevation angle given in Figure 6.

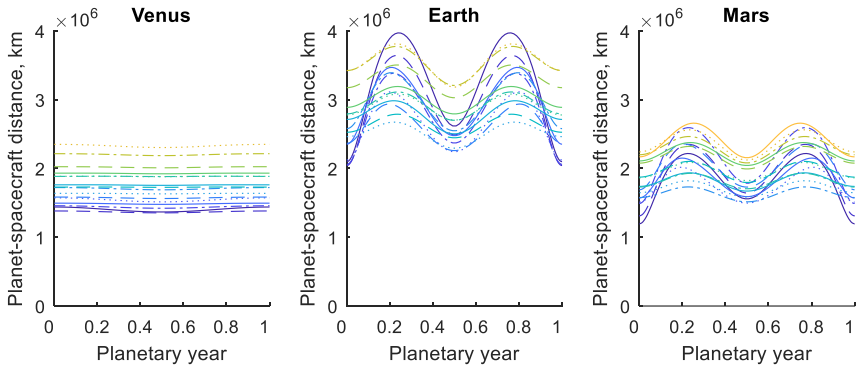

Figure 8 Planet – spacecraft distance for an ideal sail reflectance model for the pole-sitter orbits in Figure 7 (using the legend of Figure 7).

Finally, the controls required to maintain the orbits in Figure 7 appear in Figure 9 (using the same legend as in Figure 7), showing smooth controls for all cases. Furthermore, for all cases, the cone angle profiles remain within the interval 32 – 68 deg, proving that the constraint in Eq. (14) is correctly enforced. Furthermore, due to the similarity in obliquity between Earth and Mars, the

control histories for those two planets are rather similar, while the large obliquity of Venus allows for more constant cone and clock angles. Finally, when replacing the ideal sail reflectance model by the non-ideal model (i.e. using the non-ideal reflectance coefficients of Table 2), the dashed red lines in Figure 6 are obtained. From the difference between the solid and dashed lines, the effect of non-ideal reflectance properties of the sail becomes clear:

- The maximum achievable value for $\gamma_{\min}$ is reduced by 5 deg for the Venus and Earth cases and by 2.5 deg for the Mars case.
- The required lightness number to achieve a particular value for $\gamma_{\min}$ increases, on average, by 0.01, though slightly less (0.0081) for Mars.

These conclusions further underline the suitability of Mars for a pole-sitter mission.

Finally, the effect of non-ideal reflectance properties on the optimised distance to the planet is presented in Figure 10. This figure shows the planet-spacecraft distance range of the pole-sitter orbits in Figure 6 from which it can be concluded that, although non-ideal reflectance properties have some effect on the minimised distance, this effect remains limited.

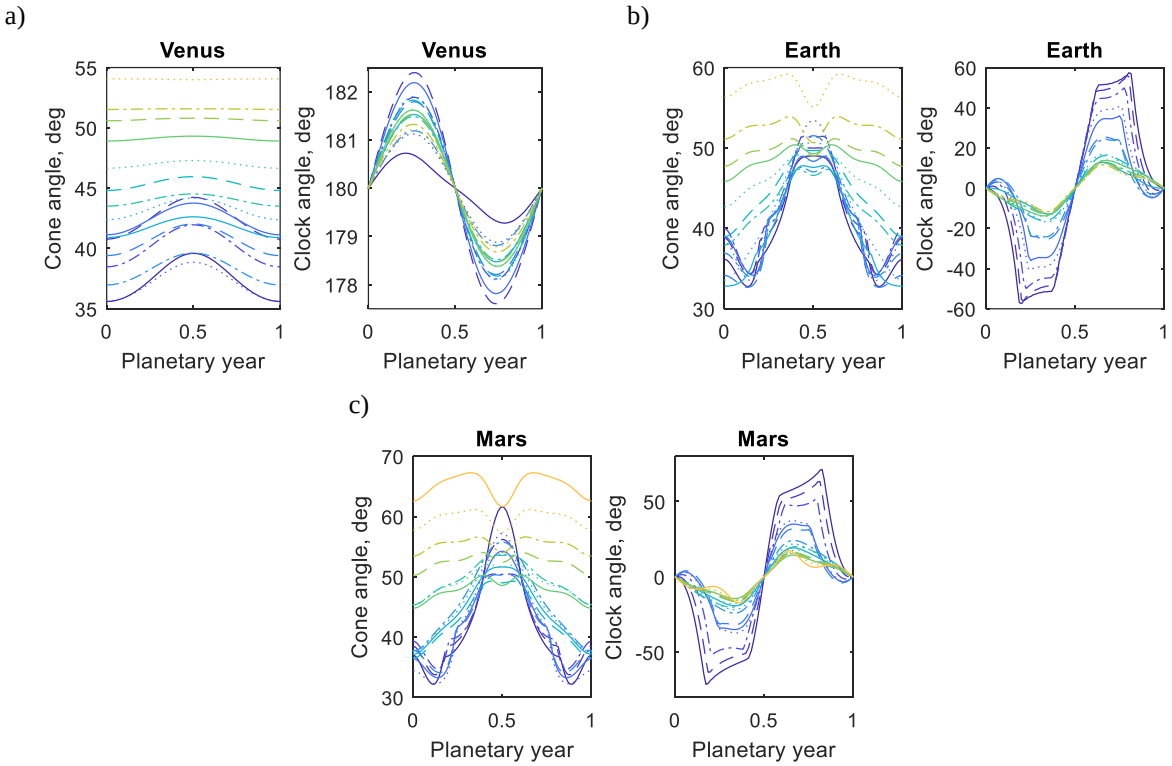

Figure 9 Sail control angles for the pole-sitter orbits in Figure 7 (using the legend of Figure 7), a) Earth case, b) Venus case, c) Mars case.

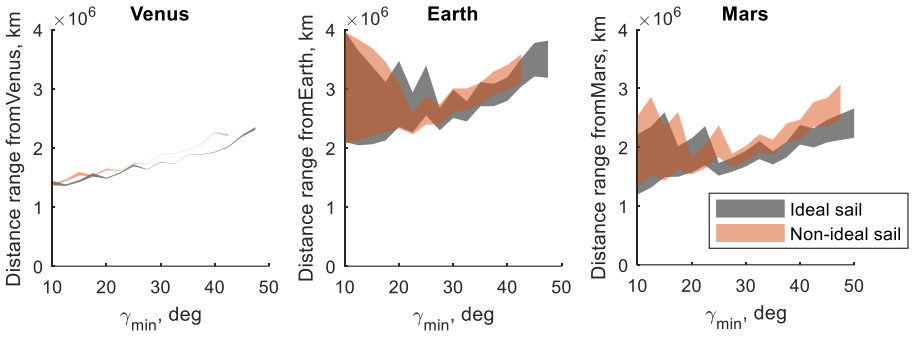

Figure 10 Comparison of the effect of the ideal and non-ideal sail reflectance models on the range of optimised planet-spacecraft distances for the pole-sitters in Figure 6.

4. Trajectory optimisation

To demonstrate the accessibility of the pole-sitter orbits designed in the previous section, this section will investigate time-optimal solar-sail transfers to those orbits. For this, it will follow the methodology outlined in (Vergaaij and Heiligers 2019), which will be summarised in Sections 4.1 – 4.3 and the results will be presented in Section 4.4.

4.1. Trajectory design approach

The aim is to find time-optimal transfers from Earth's vicinity to the pole-sitter orbits of Section 3.5. In particular, as departure condition, perigee of an Ariane V Geostationary Transfer Orbit (GTO) is assumed (Arianespace 2008). From previous research (Vergaaij and Heiligers 2019) it is known that the best results are obtained by launching from a midnight GTO (perigee located on the nightside of the Earth) for transfers to pole-sitters at Venus and from a midday GTO (perigee located on the dayside of the Earth) for transfers towards pole-sitters at Mars. For Earth, launch from a midnight GTO is assumed. At perigee of this GTO, a ΔV is applied that sends the spacecraft onto a parabolic escape trajectory. The part of the transfer from perigee of the GTO up to the sphere of influence of Earth is modelled as a ballistic (i.e. no solar-sail propulsion) two-body arc. At the sphere of influence, a switch from the two-body problem to the Sun-Earth (SE-)CRTBP is made and the sail is deployed, thereby initiating the propelled phase of the mission.

Since the pole-sitters at Venus and Mars are defined in a different CRTBP than the SE-CRTBP (the Sun-Venus (SV-) and Sun-Mars (SM-)CRTBP, respectively), the propelled phase of the mission is split into two phases: one phase ("phase 1") that makes use of the dynamics in the SE-CRTBP and a subsequent second phase ("phase 2") that makes use of the dynamics of the SV- or SM-CRTBP, depending on the targeted pole-sitter. To guarantee a continuous transfer across these phases, a smooth linkage of the two phases in terms of states, controls, and time is enforced. Finally, note that, for consistency in the approach, the transfer to the Earth pole-sitter orbits is also divided into two phases, though the dynamics across both phases are those of the SE-CRTBP.

4.2. Optimal control problem

To obtain time-optimal transfers from GTO to the pole-sitter orbits of Section 3.5, the objective is to find the spacecraft states $\mathbf{x}(\tau)=\begin{bmatrix} x & y & z & v_x & v_y & v_z \end{bmatrix}^T$ and controls $\mathbf{u}(\tau)=\begin{bmatrix} \alpha & \delta \end{bmatrix}^T$ over time, τ, that minimise the overall time spent in the transfer, while satisfying the dynamics of Eq. (1) (using the same sail reflectance model as used in the pole-sitter orbits). A minimum-time transfer will reduce mission operational cost and can be expressed through the following objective function

$$J_2 = \tau_f - \tau_0 \tag{15}$$

in which τ_f and τ_0 are the final time upon entering the pole-sitter orbit and the initial time at perigee of the GTO, respectively.

Suitable bounds on the states and controls are enforced, where the latter are the same as those defined in Eq. (14). In terms of boundary constraints, the initial state is forced to coincide with perigee of the GTO and the final state should match the position and velocity of the pole-sitter orbit at the time of entering the pole-sitter orbit. Furthermore, to ensure a smooth linkage across the phases introduced in Section 4.1, the following linkage constraints are enforced:

$$\underset{\sim}{\mathbf{x}}_{f,1} = \underset{\sim}{\mathbf{x}}_{0,2},\ \mathbf{u}_{f,1} = \mathbf{u}_{0,2},\ \underset{\sim}{\tau}_{f,1} = \underset{\sim}{\tau}_{0,2} \tag{16}$$

where the subscripts "$f,1$" and "$0,2$" refer to the final conditions of the first phase and the initial conditions of the second phase, respectively. Note that the linkage of the states occurs in an inertial heliocentric frame $I(\hat{\mathbf{x}}_I, \hat{\mathbf{y}}_I, \hat{\mathbf{z}}_I)$ where the basis vector $\hat{\mathbf{x}}_I$ points towards the Vernal Equinox, $\hat{\mathbf{z}}_I$ is oriented perpendicular to the ecliptic plane and $\hat{\mathbf{y}}_I$ completes the right-handed reference frame. In this frame, the states are denoted as $\underset{\sim}{\mathbf{x}}$. Furthermore, linkage in time occurs in MJD2000, which is denoted as $\underset{\sim}{\tau}$. Linkage of the controls does not require a transformation, because $\mathbf{u}$ is defined in the sail-centred frame B.

The optimal control problem defined in this section is solved with PSOPT. Further details on its implementation can be found in (Vergaaij and Heiligers 2019).

4.3. Initial guess

As already mentioned in Section 3.3, an initial guess is required to initialise any optimisation in PSOPT. Here, this initial guess is provided using a strategy based on the search for heteroclinic connections in dynamical systems theory (Koon, Lo, Marsden et al. 2011, Heiligers, Mingotti and McInnes 2015, Heiligers 2018). In particular, topological tubes, similar to those formed by the manifolds of periodic orbits, are created by forward and backward propagating different initial conditions along the GTO and pole-sitter orbit, where different refers to different departure and arrival times. The shape of the topological tube can be altered using different sail attitudes during the

propelled phase of the mission. When a suitable linkage between such forward and backward integrated trajectories exists, an initial guess is obtained. Note that the forward integration from GTO up until linkage of the two tubes constitutes phase 1 and is computed in the SE-CRTBP, while the backward propagation from the pole-sitter up until linkage is phase 2 and is computed in the Sun-planet CRTBP.

Using this approach, the initial guess can be defined by a discrete number of parameters: the departure time at GTO, t_{dep}, the arrival time at the pole-sitter orbit, t_{arr} the time of linkage of the forward and backward propagated trajectories (i.e. linkage of the two phases), t_{link}, and a piecewise-constant attitude of the sail in both phases. To select the correct values for these parameters, a genetic algorithm is taken at hand. The attractiveness of a genetic algorithm is the simplicity of the implementation, which is taken one step further in this work by using the *ga.m* function in Matlab® with default options, except for the initial population. Because the initial population generated within the *ga.m* function is biased towards the boundaries of the parameters, it is manually generated according to a pseudorandom uniform distribution between the defined bounds on the gene structure. This gene structure is as follows: $\mathbf{X} = \begin{bmatrix} t_{dep} & t_{arr} & t_{link} & \boldsymbol{\alpha}_1 & \boldsymbol{\delta}_1 & \boldsymbol{\alpha}_2 & \boldsymbol{\delta}_2 \end{bmatrix}^T$ where $(\boldsymbol{\alpha}_1, \boldsymbol{\delta}_1)$ and $(\boldsymbol{\alpha}_2, \boldsymbol{\delta}_2)$ are sets of cone and clock angles that are used in phases 1 and 2, respectively. Each set is subdivided into a subset of three cone and clock angles that are used across equidistant time intervals in each phase. To limit the search space for the genetic algorithm, suitable bounds are set on these parameters, for which details can be found in (Vergaaij and Heiligers 2019).

The fitness of the individuals in the population is defined as a weighted sum of the discontinuities in position, Δr, and velocity, Δv, at the linkage of the two phases:

$$J_3 = \Delta r + w \Delta v \tag{17}$$

with w a weight. Note that the actual discontinuities are computed in the inertial heliocentric reference frame introduced in Section 4.1.

Due to the inherent randomness in the genetic algorithm approach, the algorithm has been initialised with five different seed values and five different weights in the objective function in Eq. (17) have been explored. Previous work has shown that weights ranging from 10^4 to ~10^6 produce satisfying results (Vergaaij and Heiligers 2019). The most suitable initial guess selected from these different initialisations shows both a small Δv and transfer time. For all initialisations, the genetic algorithm is able to minimise Δr to the order of kms, similar to the results obtained in (Vergaaij and Heiligers 2019).

4.4. Results

To demonstrate the accessibility of the pole-sitter orbits, this section provides the time-optimal transfer results for a lightness number value of $\beta = 0.05$ and for targeting the pole-sitter orbit with the largest minimum elevation that can be achieved for $\beta = 0.05$, see Figure 6. From previous results, see (Vergaaij and Heiligers 2019), it can be expected that smaller or larger values for the lightness number will result in longer or shorter transfer times, respectively, while the actual pole-sitter orbit targeted has only a minor influence on the transfer time.

Details of the optimised results are provided in Table 4, showing the minimum elevation angle of the targeted pole-sitter orbit, the departure and arrival times, and the corresponding transfer times for all three pole-sitter cases (Venus, Earth, and Mars) and for both an ideal and non-ideal sail reflectance model. Note that the transfer times span the time from perigee of the GTO up until arrival in the pole-sitter orbit. Clearly, due to the close proximity of the Earth pole-sitter, the shortest transfer times are found for that case. Similarly, since Venus is positioned closer to Earth than Mars and due to an increase in the solar radiation pressure when travelling sunward, the transfer to the Venus pole-sitter takes approximately half the time of the transfer to the Mars pole-sitter. Furthermore, from Table 4 it can be derived that the non-specular reflectance properties of the sail add 12.3%, 6.8%, and 11.9% to the transfer times for the Venus, Earth and Mars cases, respectively. This is in line with previously reported increases in time of flight of 8 – 10.8% (Mengali and Quarta 2009, Heiligers, Diedrich, Derbes et al. 2014, Vergaaij and Heiligers 2019).

Further details on the transfers are provided in Figure 11 to Figure 13. Each figure shows the transfer in either the inertial heliocentric frame (for the Venus and Mars cases) or the Sun-Earth synodic frame (for the Earth case). Note that the arrows represent the direction and relative magnitude of the sail acceleration vector. The figures also provide the history of the sail attitude angles for both the ideal and non-ideal sail reflectance models, demonstrating that the non-ideal sail model tends to use smaller variations in the cone angles.

Table 4 Details of time-optimal transfers to pole-sitter orbits with $\beta = 0.05$: achievable minimum elevation angle, $\gamma_{\min}$, departure (t_{dep}) and arrival (t_{arr}) dates, and the total transfer time.

	Sail model	$\gamma_{\min}$, deg	t_{dep}	t_{arr}	Transfer time, days
Venus	Ideal	25	31-3-2021	27-8-2022	477.6
	Non-ideal	15	21-2-2021	17-9-2022	536.3
Earth	Ideal	30	28-4-2022	23-9-2022	111.3
	Non-ideal	20	3-5-2022	5-10-2022	118.9
Mars	Ideal	47.5	4-12-2021	15-7-2024	917.9
	Non-ideal	42.5	29-10-2021	26-9-2024	1026.5

a) b)

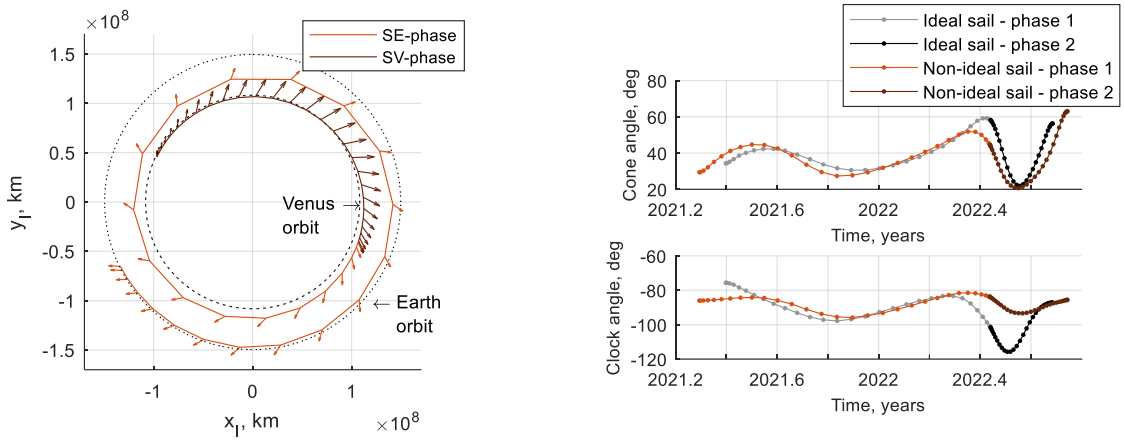

Figure 11 **Venus case**: a) time-optimal transfer for a non-ideal sail reflectance model in the inertial heliocentric frame, b) control history for an ideal and non-ideal sail reflectance model.

a) b)

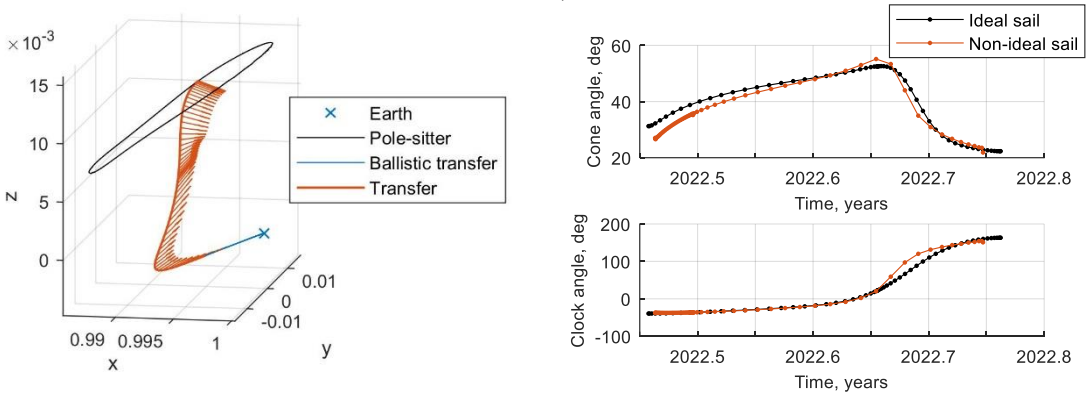

Figure 12 **Earth case**: a) time-optimal transfer for a non-ideal sail reflectance model in the Sun-Earth synodic frame, b) control history for an ideal and non-ideal sail reflectance model.

a) b)

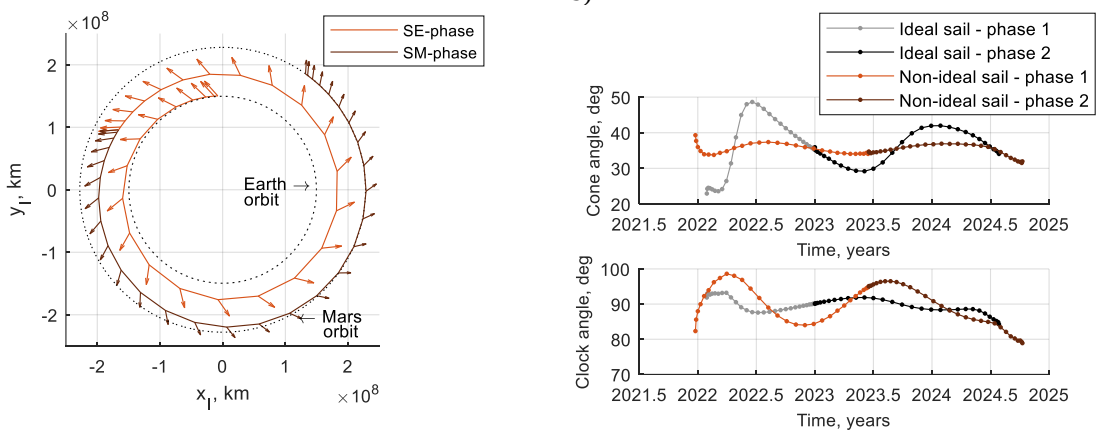

Figure 13 **Mars case**: a) time-optimal transfer for a non-ideal sail reflectance model in the inertial heliocentric frame, b) control history for an ideal and non-ideal sail reflectance model.

5. Trajectory and orbit control

The solutions for the pole-sitter orbits and transfer trajectories obtained in Sections 3 and 4 are designed using the dynamics in Eq. (1). These reference solutions therefore do not account for small dynamical perturbations nor for errors in the spacecraft guidance. To account for these effects, this section investigates the control of both the trajectory and the pole-sitter orbit using a linear quadratic regulator (LQR) implemented in MATLAB Simulink®. A similar approach has been used in previous works on the control of pole-sitter orbits, (Ceriotti and McInnes 2011, Ceriotti, Heiligers and McInnes 2014), but, while those works used a solar-electric propulsion thruster to provide the necessary control, this paper uses only the solar sail.

While designing the control strategy, the following assumptions are made:

1. The spacecraft is a perfect observer, i.e. it has perfect knowledge of its state (position and velocity).
2. The sail is assumed to have a degree of control over its area exposed to the Sun, effectively changing the lightness number (or characteristic acceleration). This can be achieved through the use of vanes, by adopting an area-changing sail configuration (e.g. a rhombic sail (Ceriotti, Harkness and McRobb 2014), by using reflectivity control devices (Mori, Shirasawa, Mimasu et al. 2013), or by adopting a heliogyro sail configuration (MacNeal 1967, Heiligers, Guerrant and Lawrence 2017)).
3. The response time and dynamics of the actuator (the sail) are neglected, which is justified by the fact that the dynamics of both the trajectory and the orbit are relatively slow.

In order to prevent saturation of the controls when using cone and clock angles, the reference control for the trajectory and pole-sitter orbit is converted to two Cartesian components of the sail normal unit vector, as:

$$\begin{cases} n_\theta = \sin\alpha \sin\delta \\ n_\varphi = \sin\alpha \cos\delta \end{cases} \tag{18}$$

These two components represent the projection of the sail normal vector, $\hat{\mathbf{n}}$, onto a plane perpendicular to the Sun line (see the left schematic in Figure 1b). The sail normal can be reconstructed from Eq. (18) considering that the remaining component is $n_r = \sqrt{1-n_\theta^2-n_\varphi^2}$.

Due to the second assumption, the reference control is expanded to include the lightness number: $\tilde{\mathbf{u}}(t) = \begin{bmatrix} \tilde{n}_\theta & \tilde{n}_\varphi & \tilde{\beta} \end{bmatrix}^T$. Note that the overtilde will from here on be used to refer to the reference solution. When the lightness number in the reference control is set to a constant value, e.g. $\tilde{\beta} = 0.05$, the reference transfer and pole-sitter orbit, $\tilde{\mathbf{x}}(t)$, are resolved.

The control is substituted into the dynamics of the "real" system (i.e. including any perturbations or errors as defined in the test cases in Section 5.2), after passing through a saturation block, which enforces the following control bounds:

$$\begin{bmatrix} -1 & -1 & \beta_{\min} \end{bmatrix}^T \leq \mathbf{u} \leq \begin{bmatrix} +1 & +1 & \beta_{\max} \end{bmatrix}^T \tag{19}$$

The values for $\beta_{\min}$ and $\beta_{\max}$ depend on the sail configuration. For example, when considering a flat sail with control vanes, the solar-sail area can be scaled up and down from the average sail area, $A+2A_{vane}$, by $2A_{vane}$, where A_{vane} is the sail area of a single vane, respectively. The lightness number will then scale proportionally with these changes in sail area. For example, following the reasoning in (Heiligers, Guerrant and Lawrence 2017), that considered a vane area of 15 m^2 for the previously proposed Sunjammer mission (Eldad and Lightsey 2014), the vanes enable an increase or decrease in the nominal sail area, and thus in the lightness number of ±2.8%. With a nominal lightness number of $\beta = 0.05$, this results in $\beta_{\min} = 0.0514$ and $\beta_{\max} = 0.0486$.

As a result of the perturbation or error, the trajectory, $\mathbf{x}(t)$, will deviate from the reference, $\tilde{\mathbf{x}}(t)$, where the error on the state, $\delta\mathbf{x}(t) = \mathbf{x}(t) - \tilde{\mathbf{x}}(t)$ is used to compute the required feedback control, $\delta\mathbf{u}(t)$. This feedback control is added to the reference control to obtain the total control, i.e. $\mathbf{u}(t) = \tilde{\mathbf{u}}(t) + \delta\mathbf{u}(t)$. This control aims to bring the trajectory back to the nominal trajectory after some time (Heiligers, Guerrant and Lawrence 2017). For small-enough errors, the system dynamics can be described through a linearisation of the dynamics in Eq. (1) around the reference trajectory and control. When writing the dynamics as a set of first-order differential equations, $\dot{\mathbf{x}}(t) = \mathbf{f}\left(\mathbf{x}(t), \mathbf{u}(t), t\right)$ and omitting the variation with time for brevity, the linearised system can be expressed in the form:

$$\delta\dot{\mathbf{x}} = \mathbf{A}\delta\mathbf{x} + \mathbf{B}\delta\mathbf{u} \tag{20}$$

with

$$\mathbf{A}_{6x6} = \left.\frac{\partial\mathbf{f}}{\partial\mathbf{x}}\right|_{\tilde{\mathbf{x}},\tilde{\mathbf{u}}}, \mathbf{B}_{6x3} = \left.\frac{\partial\mathbf{f}}{\partial\mathbf{u}}\right|_{\tilde{\mathbf{x}},\tilde{\mathbf{u}}} \tag{21}$$

The optimal control problem to be solved is then one of minimising the following quadratic cost function:

$$J_4 = \int_0^\infty \left(\delta\mathbf{x}^T\mathbf{Q}\delta\mathbf{x} + \delta\mathbf{u}^T\mathbf{R}\delta\mathbf{u}\right)dt \tag{22}$$

where the first and second terms on the right-hand side penalise the transient state error and control effort, respectively. For the weighing matrices in Eq. (22), $\mathbf{Q}_{6x6} = \text{diag}\begin{bmatrix} Q_r & Q_r & Q_r & Q_v & Q_v & Q_v \end{bmatrix}$

and $\mathbf{R}_{3x3} = \mathrm{diag}\begin{bmatrix} R & R & R \end{bmatrix}$, the three scalars Q_r, Q_v, R are optimised to maximise the convergence (see later in Section 5.1). The control that minimises the cost function in Eq. (22) is assumed linear to the state error:

$$\delta\mathbf{u} = -\mathbf{K}\delta\mathbf{x} \tag{23}$$

and leads to the well-known algebraic Riccati equation, which can be solved numerically using MATLAB® to compute the gain matrix $\mathbf{K}$. The expressions of the Jacobians in Eq. (21) are found analytically, but re-evaluated numerically at every integration step, and so is the gain matrix $\mathbf{K}$, which is therefore time-varying. The resulting control is added to the reference to find the total control.

5.1. Gain tuning

The choice for the values of the matrices $\mathbf{Q}$ and $\mathbf{R}$ substantially affects the performance of the LQR. Therefore, an accurate selection of their coefficients is fundamental. An initial guess of the coefficient values was obtained initially following Bryson's rule ($\mathbf{Q}$, $\mathbf{R}$ diagonal with $Q_i =$ inverse of the maximum acceptable value of δx_i^2, $R =$ inverse of the maximum acceptable value of u_i^2), and then the coefficients were optimised using a genetic algorithm. The objective function (to be maximised) was selected as the success rate of 50 simulations of the control, with an initial state, at the beginning of the second phase of the transfer (hence in the Sun-planet system), perturbed randomly. The simulation (and with this the control) is considered successful if the final state, after the transfer and one full pole-sitter orbit, is "close" to the reference. The actual value of the distance used is not crucial, because a divergent trajectory usually diverges very far from the reference, and it is therefore straightforward to detect.

A random normal distribution of perturbed initial states $\mathbf{x}_0$ is generated, using an ellipsoid of uncertainty of radius $r_u = 5 \times 10^{-3}$ (3σ in non-dimensional units) in the 6-dimensional state space, centred in the nominal initial state $\tilde{\mathbf{x}}_0$. Once each perturbed initial state is generated, the feedback control simulation is run, to assess whether it is possible to recover the spacecraft onto the reference trajectory.

To tune the gains, the genetic algorithm was run with a population of 20 individuals for 20 generations, for each of the three targets. As a test case, the non-ideal sail reflectance model and a lightness number $\beta = 0.05$ were considered. The gains in Table 5 were found.

Table 5 Optimal LQR gains.

	Q_r	Q_v	R
Venus	34.0259	51.3687	0.0229
Earth	19.0201	6.0375	0.0025
Mars	39.8260	68.2158	0.0042

5.2. Test cases and results

In order to assess the controllability of each trajectory, another Monte Carlo campaign was run, with 100 randomly distributed initial states. The radius of the uncertainty ellipsoid was set to three different values, to represent small, medium and large errors. The base radius is $r_u = 8.7289 \times 10$ (corresponding to approximately 130,000 km and 10% of the velocity of the Earth pole-sitter), with the other two defined as 2 and 3 times the base value.

Figure 14 shows the success rate of the Monte Carlo campaign for the three targets, and size of perturbations, when the perturbation is applied at the beginning of the second phase of the transfer. The Mars and Venus trajectories are very robust, with 100% success rate for the small perturbation. The Earth case, instead, is more sensitive, with a slightly smaller success rate. As expected, the success rate decreases for larger perturbation radii.

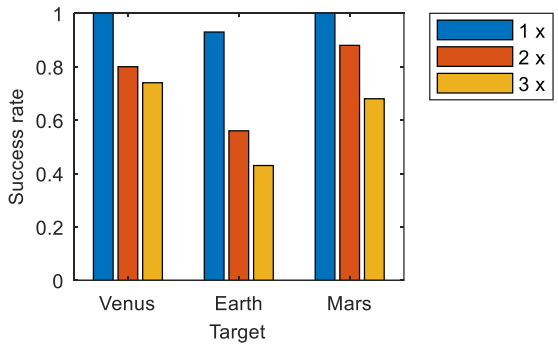

Figure 14 Success rate for three radii of the sphere of uncertainty r_u on the initial conditions at the beginning of the second phase of the transfer.

Figure 15 shows an example of a controlled trajectory for Venus. In Figure 15a, one successfully controlled trajectory and an unsuccessful one are shown. It can be noticed that the initial state error is much larger for the unsuccessful one. On the other hand, the successful trajectory highlights how the error with respect to the reference, $\delta\mathbf{x}$, is considerably reduced only after reaching the vicinity of the pole-sitter orbit, and not during the transfer (see Figure 15b and Figure 15c).

Finally, Figure 15d shows the control: the top plot represents (instead of the sail cone and clock) the tilt angle with respect to the reference: this can be an indicator of the amount of sail steering required by the feedback control with respect to the reference. We note that the tilt is mostly below 20 deg, apart from a spike to 60 deg; this happens at the pole-sitter injection point, and is due to the

sudden change in reference control. In the bottom plot, the required variation of sail area (in terms of lightness number) is shown. The saturation of this control to the limit set of ±2.8% is very evident for the great part of the trajectory, until the state error is considerably reduced. It is important to underline that, even if the variation in sail area is minor, it plays an essential role in the controllability of the trajectories.

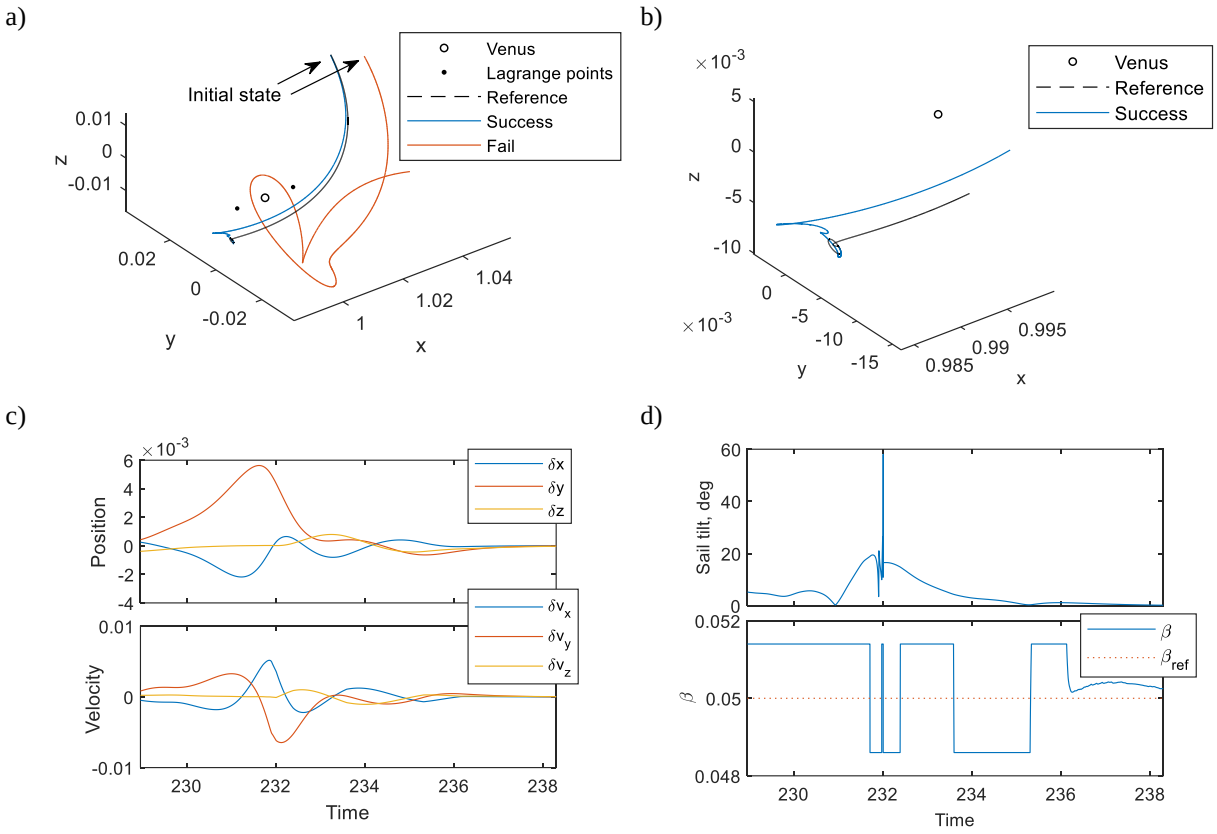

Figure 15 **Venus case**: feedback control, perturbation applied at the beginning of the second phase of the transfer. A) Examples of successfully and unsuccessfully controlled trajectories, b) magnification around the pole-sitter orbit, c) state error $\delta\mathbf{x}$, d) control.

Figure 16 is similar to the previous case, however now the perturbation is applied at injection into the pole-sitter orbit. This is a critical point as it is where the transfer trajectory matches the pole-sitter orbit, and there is a discontinuity in the controls, as well as a rapid change of states, in the reference solution. The results are therefore very different quantitatively, with Venus being the most controllable scenario, while Mars being the most critical. In particular, for Mars, the success rate is very low, and the slightly higher rate of the "3×" case, with respect to the "2×" case, is not statistically significant.

Finally, as further example, Figure 17a shows one successfully-controlled trajectory for the Earth case and one with larger initial perturbation, where the control fails. Figure 17b shows the control effort; in this case, the sail tilt remains limited to 8 deg. A control instability on the sail area is visible

in the bottom plot; this is a consequence of the automatic optimisation of the gains, and it is likely that it can be removed by fine-tuning those affecting specifically this control.

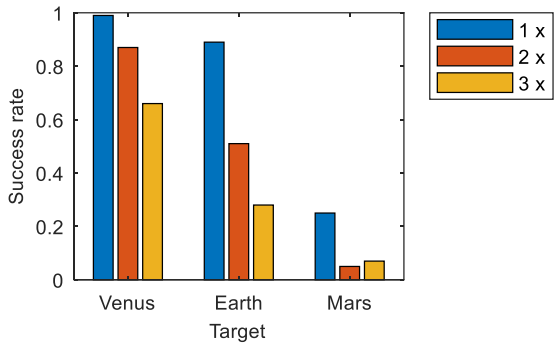

Figure 16 Success rate for three radii of the sphere of uncertainty r_u on the initial conditions at pole-sitter orbit insertion.

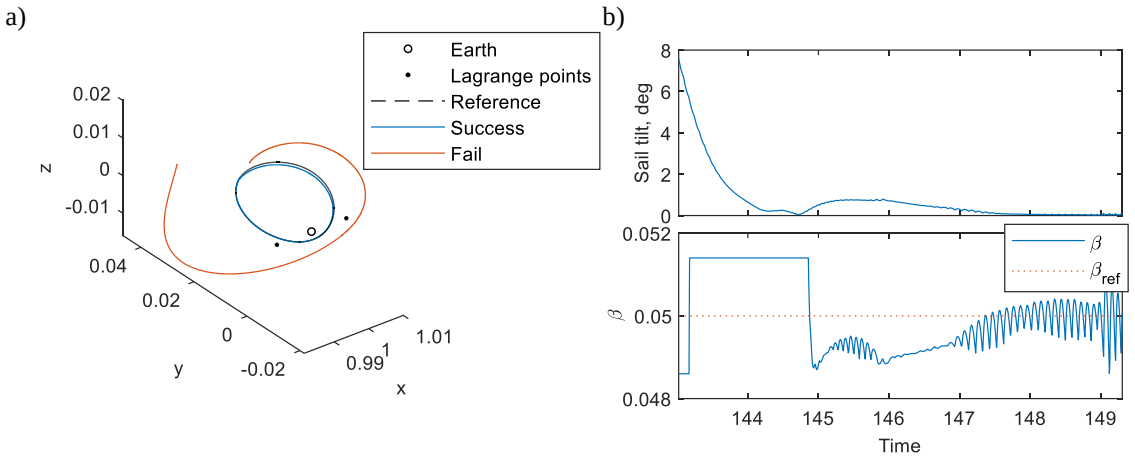

Figure 17 **Earth case**: feedback control, perturbation applied at pole-sitter injection. a) Reference trajectory, and examples of successfully and unsuccessfully controlled trajectories, b) control.

6. Conclusions

In this paper, an approach has been presented to successfully obtain solar-sail-only pole-sitter orbits at Venus, Earth, and Mars. Through the use of solar-sail propulsion only, in contrast to previous work that relied on a hybridisation of solar-sail and solar-electric propulsion, these orbits can be maintained, in theory, indefinitely, only limited by the lifetime of the sail. The found pole-sitter orbits allow to maintain a spacecraft above the planet's polar regions while achieving a continuous view of any location above a latitude of 65.8 deg (latitude of the Earth's Arctic circle) at a certain minimum elevation angle. The larger this minimum elevation angle, the better the quality of the observations, but also the larger the required lightness number of the sail. Minimum elevation angles of 10 to 50 deg have been obtained for solar-sail lightness numbers in the range 0.01 – 0.1. For Mars, relatively small lightness numbers can already achieve large elevation angles: for example, at Mars,

a lightness number of 0.05 can achieve an elevation angle of 47.5 deg, while at Venus and Earth the same lightness number only provides elevation angles above 25 and 30 deg, respectively. This result suggests that Mars is a highly suitable planet for a pole-sitter mission. In addition, through a comparison of the orbits for an ideal and non-ideal sail reflectance model, it appears that the performance of the orbits at Mars are the least affected by non-ideal properties of the sail. However, Mars does require the longest transfer time (918 days for an ideal sail) to reach the pole-sitter orbits starting from perigee of a geostationary transfer orbit: twice as long as the transfer to Venus and approximately eight times as long as the transfer to an Earth pole-sitter. The effect of non-ideal reflectance properties of the sail is in this case an increase in the transfer time of 11.8% for Mars and 12.3% and 6.8% for the Earth and Venus cases, respectively. In terms of trajectory control, early errors in the transfer are very likely to be controlled and recovered from, with reasonable control effort. Instead, the targeting of the pole-sitter orbit must be much more accurate, in order to avoid loss of the spacecraft. This is particularly critical for the Mars scenario.

Acknowledgments

Merel Vergaaij gratefully acknowledges the College of Science and Engineering (University of Glasgow) for supporting this work, and the Royal Aeronautical Society and Women in Aerospace - Europe for support to attend the 5th International Symposium on Solar Sailing.

Matteo Ceriotti would like to thank the James Watt School of Engineering (University of Glasgow) and the Institution of Mechanical Engineers (IMechE Conference Grant EAC/KDF/OFFER/19/046) for supporting this work.

References

Arianespace (2008). Ariane 5 User's Manual - Issue 5 - Revision 0.

Baoyin, H. and C. McInnes (2006). "Solar Sail Halo Orbits at the Sun-Earth Artificial L1-point." Celestial Mechanics and Dynamical Astronomy **94**: pp. 155-171, doi: 10.1007/s10569-005-4626-3.

Becerra, V. M. (2010). Solving Complex Optimal Control Problems at No Cost with PSOPT. In: Proceedings of the IEEE Multi-conference on Systems and Control, Yokohama, Japan, pp. 1391-1396.

Biddy, C. and T. Svitek (2012). LightSail-1 Solar Sail Design and Qualification. Presentation at Proceedings of the 41st Aerospace Mechanisms Symposium, Pasadena, CA.

Ceriotti, M., P. Harkness and M. McRobb (2014). Variable-Geometry Solar Sailing: The Possibilities of the Quasi-Rhombic Pyramid. Advances in Solar Sailing. M. Macdonald. Berlin, Heidelberg, Springer Berlin Heidelberg**:** 899-919.

Ceriotti, M., J. Heiligers and C. R. McInnes (2014). "Trajectory and Spacecraft Design for a Pole-Sitter Mission." Journal of Spacecraft and Rockets **51**(1): pp. 311-326, doi: 10.2514/1.A32477.

Ceriotti, M. and C. R. McInnes (2010). Hybrid Solar Sail and SEP Propulsion for Novel Earth Observation Missions. Presentation at 61st International Astronautical Congress, Prague, Czech Republic.

Ceriotti, M. and C. R. McInnes (2011). "Generation of Optimal Trajectories for Earth Hybrid Pole Sitters." Journal of Guidance, Control, and Dynamics **34**(3): pp. 847-859, doi: 10.2514/1.50935.

Ceriotti, M. and C. R. McInnes (2011). "Hybrid Solar Sail and Solar Electric Propulsion for Novel Earth Observation Missions." Acta Astronautica **69**(9-10): pp. 809-821, doi: 10.1016/j.actaastro.2011.06.007.

Dachwald, B. (2005). "Optimal Solar Sail Trajectories for Missions to the Outer Solar System." Journal of Guidance, Control, and Dynamics **28**(6): pp. 1187-1193, doi: 10.2514/1.13301.

Driver, J. (1980). "Analysis of an Arctic Polesitter." Journal of Spacecraft and Rockets **17**(3): pp. 263-269, doi: 10.2514/3.57736.

Eldad, O. and E. G. Lightsey (2014). Attitude Control of the Sunjammer Solar Sail Mission. Proceedings of the AIAA/USU Conference on Small Satellites, Logan, Utah, USA, SSC14-X-4, https://digitalcommons.usu.edu/smallsat/2014/Propulsion/3/.

Golan, O. M. and J. V. Breakwell (1988). Low Thrust Power-Limited Transfer For a Pole Squatter. Presentation at AIAA/AAS Astrodynamics Conference, Minneapolis, Minnesota.

Grebow, D. J., M. T. Ozimek and K. C. Howell (2008). "Multibody Orbit Architectures for Lunar South Pole Coverage." Journal of Spacecraft and Rockets **45**(2): pp. 344-358, doi: 10.2514/1.28738.

Heaton, A., N. Ahmad and K. Miller (2017). Near Earth Asteroid Scout Solar Sail Thrust and Torque Model (17055). Proceedings of the 4th International Symposium on Solar Sailing, Kyoto, Japan.

Heiligers, J. (2018). "Homo- and Heteroclinic Connections in the Planar Solar-Sail Earth-Moon Three-Body Problem." Frontiers in Applied Mathematics and Statistics, 4: pp. 42, doi: 10.3389/fams.2018.00042.

Heiligers, J., M. Ceriotti, C. R. McInnes and J. D. Biggs (2012). "Design of Optimal Earth Pole-Sitter Transfers Using Low-Thrust Propulsion " Acta Astronautica **79**: pp. 253-268, doi: 10.1016/j.actaastro.2012.04.025.

Heiligers, J., M. Ceriotti, C. R. McInnes and J. D. Biggs (2012). Design of Optimal Transfers Between North and South Pole-Sitter Orbits. Presentation at 22nd AAS/AIAA Space Flight Mechanics Meeting, Charleston, SC.

Heiligers, J., M. Ceriotti, C. R. McInnes and J. D. Biggs (2014). "Mission Analysis and Systems Design of a Near-Term and Far-Term Pole-Sitter Mission." Acta Astronautica **94**(1), pp. 455-469 doi: 10.1016/j.actaastro.2012.12.015.

Heiligers, J., B. Diedrich, B. Derbes and C. R. McInnes (2014). Sunjammer: Preliminary End-to-End Mission Design. Presentation at 2014 AIAA/AAS Astrodynamics Specialist Conference, San Diego, CA, USA.

Heiligers, J., J. M. Fernandez, O. R. Stohlman and K. W. Wilkie (2019). "Trajectory Design for a Solar-Sail Mission to Asteroid 2016 HO3." Astrodynamics **3**(3): pp. 231-246, doi: 10.1007/s42064-019-0061-1.

Heiligers, J., D. Guerrant and D. Lawrence (2017). "Exploring the Heliogyro's Orbital Control Capabilities for Solar Sail Halo Orbits." Journal of Guidance, Control, and Dynamics **40**(10): pp. 2569-2586, doi: 10.2514/1.G002184.

Heiligers, J., G. Mingotti and C. R. McInnes (2015). "Optimal Solar Sail Transfers Between Halo Orbits of Different Sun-Planet Systems." Advances in Space Research **55**(5): pp. 1405-1421, doi: j.asr.2014.11.033.

Heiligers, J., T. D. van den Oever, M. Ceriotti, P. Mulligan and C. R. McInnes (2017). Continuous planetary polar observation from hybrid pole-sitters at Venus, Earth, and Mars. Proceedings of the 4th International Symposium on Solar Sailing, Kyoto, Japan.

Howell, K. C. (1983). "Three-Dimensional, Periodic, 'Halo' Orbits." Celestial Mechanics and Dynamical Astronomy **32**: pp. 53-71, doi: 10.1007/BF01358403.

Johnson, L., M. Whorton, A. Heaton, R. Pinson, G. Laue and C. Adams (2011). "NanoSail-D: A Solar Sail Demonstration Mission." Acta Astronautica **68**: pp. 571-575, doi: 10.1016/j.actaastro.2010.02.008.

Koon, W. S., M. W. Lo, J. E. Marsden and S. D. Ross (2011). Dynamical Systems, the Three-Body Problem and Space Mission Design, Springer New York.

MacNeal, R. H. (1967). The Heliogyro - an Interplanetary Flying Machine (Report: NASA-CR-84460). United States.

McInnes, C. R. (1999). Solar Sailing: Technology, Dynamics and Mission Applications. Berlin, Springer-Verlag.

Mengali, G. and A. A. Quarta (2009). "Solar Sail Trajectories with Piecewise-Constant Steering Laws." Aerospace Science and Technology **13**: pp. 431-441, doi: 10.1016/j.ast.2009.06.007.

Mori, O., Y. Shirasawa, Y. Mimasu, Y. Tsuda, H. Sawada, T. Saiki, T. Yamamoto, K. Yonekura, H. Hoshino, J. Kawaguchi and R. Funase (2014). Overview of IKAROS Mission. Advances in Solar Sailing. M. Macdonald. Berlin, Heidelberg, Springer Berlin Heidelberg: pp. 25-43

Vergaaij, M. and J. Heiligers (2019). "Solar-Sail Trajectory Design to Planetary Pole Sitters." Journal of Guidance, Control, and Dynamics **42**(6): pp. 1402-1412, doi: 10.2514/1.g003952.

Wächter, A. and L. T. Biegler (2006). "On the Implementation of an Interior-point Filter Line-search Algorithm for Large-scale Nonlinear Programming." Mathematical Programming **106**(1): pp. 25-57, doi: 10.1007/s10107-004-0559-y.

Walmsley, M., J. Heiligers, M. Ceriotti and C. McInnes (2016). "Optimal Trajectories for Planetary Pole-Sitter Missions." Journal of Guidance, Control, and Dynamics **39**(10): pp. 2461-2468, doi: 10.2514/1.G000465.

Waters, T. J. and C. R. McInnes (2007). "Periodic Orbits Above the Ecliptic in the Solar-Sail Restricted Three-Body Problem." Journal of Guidance, Control, and Dynamics **30**(3): pp. 687-693, doi: 10.2514/1.26232.

McInnes, C. R. (1999). Solar Sailing: Technology, Dynamics and Mission Applications. Berlin, Springer-Verlag.

Mengali, G. and A. A. Quarta (2009). "Solar Sail Trajectories with Piecewise-Constant Steering Laws." Aerospace Science and Technology **13**: pp. 431-441, doi: 10.1016/j.ast.2009.06.007

Mori, O., Y. Shirasawa, Y. Mimasu, Y. Tsuda, H. Sawada, T. Saiki, T. Yamamoto, K. Yonekura, H. Hoshino, J. Kawaguchi and R. Furnase (2013). Overview of IKAROS Mission. Third International Symposium on Solar Sailing, Glasgow, UK, Springer Berlin Heidelberg.

Vergaaij, M. and J. Heiligers (2019). "Solar-Sail Trajectory Design to Planetary Pole Sitters." Journal of Guidance, Control, and Dynamics **42**(6): pp. 1402-1412, doi: 10.2514/1.g003952.

Wächter, A. and L. T. Biegler (2006). "On the Implementation of an Interior-point Filter Line-search Algorithm for Large-scale Nonlinear Programming." Mathematical Programming **106**(1): pp. 25-57, doi: 10.1007/s10107-004-0559-y.

Walmsley, M., J. Heiligers, M. Ceriotti and C. McInnes (2016). "Optimal Trajectories for Planetary Pole-Sitter Missions." Journal of Guidance, Control, and Dynamics **39**(10): pp. 2461-2468, doi: 10.2514/1.G000465.

Waters, T. J. and C. R. McInnes (2007). "Periodic Orbits Above the Ecliptic in the Solar-Sail Restricted Three-Body Problem." Journal of Guidance, Control, and Dynamics **30**(3): pp. 687-693, doi: 10.2514/1.26232.